



23 generally divided into surface and underground double-layered structures. The parameters
24 that represent the structural functions of each layer have clear physical meanings, and the
25 parameters are less than those of the current distributed models. This allows modeling in
26 karst areas with only a small amount of necessary hydrogeological data. 18 flood processes
27 across the karst underground river in the Qingmuguan karst trough valley are simulated by
28 the QMG model, and the simulated values agree well with observations, for which the
29 average value of Nash–Sutcliffe coefficient was 0.92. A sensitivity analysis shows that the
30 infiltration coefficient, permeability coefficient, and rock porosity are the parameters that
31 require the most attention in model calibration and optimization. The improved
32 predictability of karst flooding by the proposed QMG model promotes a better mechanistic
33 depicting of runoff generation and confluence in karst trough valleys.

34 **Keywords:** Simulation and forecasting of karst floods; Karst trough valleys; QMG
35 (Qingmuguan) model; Parametric optimization; Parameter sensitivity analysis

36 **1. Introduction**

37 Karst trough valleys are very common in China, especially in the southwest. In general,
38 these karst areas are water scarce because their surfaces store very little rainfall, but it is also
39 a potential birthplace for floods. Because trough and valley landforms and topographic
40 features facilitate the formation and propagation of floods (Li et al., 2021). Taking the study
41 area, the Qingmuguan karst trough valley for example, floods used to happen here
42 constantly. In recent years, with the increase in extreme rainfall events and the increased
43 area of construction land in the region, rainfall infiltration decreased as long as rapid runoff
44 over impervious surfaces increased that results in frequent catastrophic flooding in the basin
45 (Liu et al., 2009). Excess water overflows from karst sinkholes and underground river
46 outlets often occur during floods, flooding large areas of farmland and residential areas and
47 causing serious economic losses (Yu et al., 2020). Therefore, the simulation and prediction



48 of karst flooding events in these karst trough valleys like the study area are both important
49 and urgently needed.

50 Hydrological models can be effective for forecasting floods and evaluating water
51 resources in karst areas (Ford and Williams, 2007; Williams, 2009). However, modeling
52 floods in karst regions is extremely difficult because of the complex hydrogeological
53 structure. Karst water-bearing systems consist of multiple media under the influence of
54 complex karst development dynamics (Worthington et al., 2000; Kovács and Perrochet,
55 2008), such as karst caves, conduits, fissures, and pores, and are usually highly spatially
56 heterogeneous (Chang and Liu, 2015; Mario et al., 2019). In addition, the intricate surface
57 hydrogeological conditions and the hydrodynamic conditions inside the karst water-bearing
58 medium result in significant temporal and spatial differences in the hydrological processes in
59 karst areas (Geyer et al., 2008; Bittner et al., 2020).

60 Early studies on flood forecasting in karst regions, with simplified lumped hydrological
61 models, were commonly used to describe the rainfall–discharge relationship (e.g., Kovács
62 and Sauter, 2007; Fleury et al., 2007b; Jukić and Denić, 2009; Hartmann et al., 2014a). With
63 the development of physical exploration technology and the progress made in mathematics,
64 computing, and other interdisciplinary disciplines, the level of modeling has gradually
65 improved (Hartmann and Baker, 2017; Hartmann, 2018; Petrie et al., 2021). Distributed
66 hydrological models have subsequently become widely used in karst areas. The main
67 difference between the lumped and distributed hydrological models is that the latter divide
68 the entire basin into many sub-basins to calculate the runoff generation and confluence,
69 thereby better describing the physical properties of the hydrological processes inside the
70 karst water-bearing system (Hartmann, 2018; Epting et al., 2018).

71 Because of their simple structure and little demand for modeling data, lumped
72 hydrological models have been used widely in karst areas (Kurtulus and Razack, 2007;
73 Ladouche et al., 2014). In a lumped model, the river basin is considered as a whole to
74 calculate the runoff generation and confluence, and there is no division running into
75 sub-basins (Dewandel et al., 2003; Bittner et al., 2020). Lumped models usually consider the
76 inputs and outputs of the model (Liedl and Sauter, 2003; Hartmann and Baker, 2013, 2017).



77 In addition, most of the model parameters are not optimized in a lumped model, and the
78 physical meaning of each parameter is unclear (Chen, 2009; Bittner et al., 2020).

79 Distributed hydrological models are of active interest in flood simulation and
80 forecasting research (Ambrose et al., 1996; Beven and Binley, 2006; Zhu and Li, 2014).
81 Compared with a lumped model, a distributed model has a more definite physical
82 significance for the model structure in terms of its mechanism (Meng and Wang, 2010;
83 Epting et al., 2018). In a distributed hydrological model, an entire karst basin can be divided
84 into many sub-basins (Birk et al., 2005) using high-resolution digital elevation map (DEM)
85 data. In the rainfall-runoff algorithm of the model, the hydrogeological conditions and karst
86 aquifer characteristics can be fully considered to precisely simulate the runoff generation
87 and confluence (Gang et al., 2019). The commonly used basin distributed hydrological
88 models (i.e., not a special groundwater numerical model such as MODFLOW) have also
89 been applied widely in karst areas, and include the SHE/MIKE SHE model (Abbott et al.,
90 1986a,b; Doummar et al., 2012), SWMM model (Peterson and Wicks, 2006; Blansett and
91 Hamlett, 2010; Blansett, 2011), TOPMODEL (Ambrose et al., 1996; Suo et al., 2007; Lu
92 et al., 2013; Pan, 2014), and SWAT model (Peterson and Hamlett, 1998; Ren, 2006).

93 The commonly used distributed hydrological models have multiple structures and
94 numerous parameters (Lu et al., 2013; Pan, 2014), which make distributed model may need
95 vast amounts of data to build its framework in karst regions. For example, the distributed
96 groundwater model MODFLOW-CFPM1 requires detailed data regarding the distribution of
97 karst conduits in a study area (Reimann et al., 2009; Qin and Jiang, 2014). Another example
98 is the Karst–Liuxihe model (Li et al., 2019), which has 5 underground vertical layers in the
99 model structure and has 15 parameters, make it hard to model in karst areas. In addition, a
100 special borehole pumping test may be required to obtain the rock permeability coefficient.

101 To overcome the difficulty of the large modeling-data demands for distributed
102 hydrological models in karst areas, a new physical model based on distributed hydrological
103 known as the QMG (Qingmuguan) model was developed. This QMG model has a
104 double-layer structure and fewer parameters. The horizontal structure is divided into river
105 channel units and slope units. The vertical structure below the surface is divided into a



106 shallow karst aquifer and a deep karst aquifer system. Only a small amount of
107 hydrogeological data is needed for modeling in karst basins.

108 To ensure that the QMG model work well in karst flood simulation and prediction in the
109 case of relatively simple structure and parameters. We carefully designed the algorithms of
110 runoff generation and confluence in the model. And to verify its applicability of QMG model
111 in flood simulation in karst basins, we selected the Qingmuguan karst trough valley in
112 Chongqing, China, as the study area for a flood simulation and uncertainty analysis. In
113 particular, the sensitivity of model parameters was analyzed.

114 2. Study Area and Data

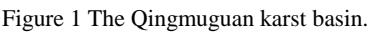
115 2.1. Landform and topography

116 The Qingmuguan karst trough valley is located in the southeastern part of the Sichuan
117 Basin, China, at the junction of the Beibei and Shapingba districts in Chongqing, with
118 coordinates of 29°40'N ~ 29°47'N, 106°17'E ~ 106°20'E. The basin covers an area of 13.4
119 km² and is part of the southern extension of the anticline at Wintang Gorge in the Jinyun
120 Mountains, with the anticlinal axis of Qingmuguan located in a parallel valley in eastern
121 Sichuan (Yang et al., 2008). The surface of the anticline is heavily fragmented, and faults
122 are extremely well-developed with large areas of Triassic carbonate rocks exposed. Under
123 the long-term erosion of karst water, a typical karst landform pattern of "three mountains
124 and two troughs" has formed (Liu et al., 2009). Such karst trough landform provides
125 convenient conditions for flood propagation, and the karst landform development is
126 extremely common in the karst region of southwest China, especially in the karst region of
127 Chongqing. Similar regions include the karst trough valley of the Zhongliang Mountains and
128 the Laolongdong karst basin in Nanshan, Chongqing.

129 The basin is oriented north-north-east and south-south-west in a narrow band of slightly
130 curved arcs and is about 12 km long from north to south. The direction of the mountains in
131 the region is basically the same as the direction of the tectonic line. The difference in
132 relative elevation is between 200–300 m. Fig.1 is a map showing an overview of the



133 Qingmuguan karst basin.

134  Figure 1 The Qingmuguan karst basin.

135 2.2. Hydrogeological conditions

136 The Qingmuguan basin is located within the subtropical humid monsoon climate zone,
137 with an average temperature of 16.5°C and a average precipitation of 1250 mm that is
138 mainly concentrated in May-September. An underground river system has developed in the
139 karst trough valley, with a length of 7.4 km, the water supply of underground river mainly
140 comes from rainfall recharge (Zhang, 2012). Most of the precipitation is collected along the
141 hill slope into the karst depressions at the bottom of the trough valley, where it is recharged
142 to the underground river through the dispersed infiltration of surface karst fissures and
143 concentrated injection from sinkholes (Fig. 1a). An upstream surface river collects in a
144 gentle valley and enters the underground river through the Yankou sinkhole (elevation 524
145 m). Surface water in the middle and lower reaches of the river system mainly enters the
146 underground river system through catenuliform sinkholes or fissures.

147 The stratigraphic and lithologic characteristics of the basin are largely dominated by
148 carbonate rocks of the Lower Triassic Jialingjiang Group (T_{1j}) and Middle Triassic Leikou
149 Slope Group (T_{2l}) on both sides of the slope, with some quartz sandstone and mudstone
150 outcrops of the Upper Triassic Xujiahe Group (T_{3xj}) (Zhang, 2012). The topography of the
151 basin presents a general anticline (Fig. 1b), where carbonate rocks on the surface are
152 corroded and fragmented, with a large permeability coefficient. Compared with the core of
153 the anticline, the rocks of the two wings of the anticline are less eroded and form a good
154 waterproof layer.

155 To investigate the karst conduits distribution in the underground river system, we
156 conducted a tracer test in the study area. The tracer was placed into the Yankou sinkhole and
157 recovered in the Jiangjia spring (Fig. 1a,c). According to the tracer test results (Gou et al.,
158 2010), the karst water-bearing medium in the aquifer was anisotropic, whereas the soluble
159 carbonate rocks were extremely permeable. The karst conduits in the underground river



160 were extremely well-developed, and there was a large single-channel underground river. The
161 response time of the underground river to rainfall was very fast, with the peak flow observed
162 at the outlet of Jiangjia spring 6–8 hours after rainfall. The flood peak rose quickly and the
163 duration of the peak flow was short. The underground river system in the study area is
164 dominated by large karst conduits, which is not conducive to water storage in water-bearing
165 media, but is very conducive to the propagation of floods.

166 2.3. Data

167 To build the QMG model to simulate the karst flood events, the necessary modelling
168 baseline data had to be collected, including: 1) high-resolution DEM data and
169 hydrogeological data (e.g., the thickness of the epikarst zone, rainfall infiltration coefficient
170 on different karst landforms, and permeability coefficient of rock); 2) land-use and soil type
171 data; and 3) rainfall data in the basin and water flow data of the underground river. The
172 DEM data was downloaded from a free database on the public Internet, with an initial spatial
173 resolution of 30×30 m. The spatial resolution of landuse and soil types were 1000×1000
174 m, and they were also downloaded from the Internet. After considering the applicability of
175 modelling and computational strength, as well as the size of the basin in the study area (13.4
176 km^2), the spatial resolution of the three types of data was resampled uniformly in the QMG
177 model and downscaled to 15×15 m based on a spatial discrete method by Berry et. (2010).

178 The hydrogeological data necessary for modelling was obtained in three simple ways. 1)
179 A basin survey was conducted to obtain the thickness of the epikarst zone, which was
180 achieved by observing the rock formations on hillsides following cutting for road
181 construction. Information was collected regarding the location, general shape, and size of
182 karst depressions and sinkholes, which had a significant impact on compiling the DEM data
183 and determining the convergence process of surface runoff. 2) Empirical equations
184 developed for similar basins were used to obtain the rainfall infiltration coefficient for
185 different karst landforms and the permeability coefficient of rock. For example, the rock
186 permeability coefficient was calculated based on an empirical equation from a pumping test
187 in a coal mine in the study area (Li et al., 2019). 3) A tracer experiment was conducted in the



188 study area (Gou et al., 2010) to obtain information on the underground river direction and
189 flow velocity.

190 Rainfall and flood data are important model inputs, and represent the driving factors
191 that allow hydrological models to operate. In the study area, rainfall data was acquired by
192 two rain gauges located in the basin (Fig. 1a). Point rainfall was then spatially interpolated
193 into basin-level rainfall (for such a small basin area rainfall results obtained from two rain
194 gauges was considered representative). There were 18 karst flood events in the period of 14
195 April 2017 to 10 June 2019. We built a rectangular open channel at the underground river
196 outlet and set up a river gauge on it (Fig. 1a) to record the water level and flow data every 15
197 minutes.

198 **3. Methodology**

199 **3.1. Hydrological model**

200 The hydrological model developed in this study was named the QMG model after the
201 basin for which it was developed and to which it was first applied, i.e., the Qingmuguan
202 basin. The QMG model proposed in this study has a two-layer structure, including a surface
203 part and an underground part, with the former mainly performing the calculation of runoff
204 generation and the confluence of the surface river, while the latter performs the confluence
205 calculation of the underground river system.

206 The structure of the QMG model is divided into a two-layer structure, both horizontally
207 and vertically. The horizontal structure of the model is divided into river channel units and
208 slope units. The vertical structure below the surface is divided into a shallow karst aquifer
209 (including soil layers, karst fissures, and conduit systems in the epikarst zone) and a deep
210 karst aquifer system (rock stratum and underground river system). This relatively simple
211 model structure makes it need only a small amount of hydrogeological data when modeling
212 in karst regions. Fig. 2 shows a flowchart of the modeling and calculation procedures
213 required for the QMG model.

214 **Figure 2 Modeling flow chart of QMG (Qingmuguan) model.**

215 To accurately describe the runoff generation and confluence on a grid scale, these karst



216 sub-basins are further divided into a lot of karst hydrological response units (KHRUs). The
 217 specific steps involved in the division were adopted by referring to studies of hydrological
 218 response units (HRUs) in TOPMODEL by Pan (2014). As the smallest basin computing
 219 units, the KHRUs can effectively ignore the spatial differences of karst development within
 220 the units and reduce the uncertainty in the classification of model units. Fig. 3 shows the
 221 spatial structure of the KHRUs.

222  Figure 3 Spatial structure of the KHRUs (Li et al., 2021).

223 The modeling and operation of the QMG model consists of three main stages: 1) spatial
 224 interpolation, and the retention of rainfall and evaporation calculations; 2) runoff generation
 225 and confluence calculation for the surface river; and 3) confluence calculation for the
 226 underground runoff, including the confluence in the shallow karst aquifer and the
 227 underground river system.

228 3.1.1. Rainfall and evaporation Calculation

229 In the QMG model, the spatial interpolation of rainfall is accomplished by a kriging
 230 method using the ArcGIS 10.2 software. The Tyson polygon method may be a simpler
 231 method for rainfall interpolation if the number of rainfall gauges in the basin is sufficient.
 232 The point rainfall observed by the two rainfall gauges in the basin (Figure 1a) was spatially
 233 interpolated into areal rainfall for the entire basin.

234 Basin evapotranspiration in the KHRUs was mainly vegetal, soil evaporation, and water
 235 surface evaporation. They were calculated using the following equations (modified from Li
 236 et al., 2020):

$$\begin{cases}
 E_v = V^{t+\Delta t} - V^t - P_v \\
 E_s = \lambda E_p, \text{ if } F = F_c \\
 E_s = \lambda E_p \frac{F}{F_c}, \text{ if } F < F_{\text{sat}} \\
 E_w = \Delta e \cdot [1.12 + 0.62(\Delta T)^{0.9}] \cdot [0.084 + 0.24(1 - \gamma^2)^{1/2}] \cdot [0.348 + 0.5\omega^{1.8-1.137\omega^{0.05}}]
 \end{cases} \quad (1)$$

238 Here, E_v [mm] is the vegetal discharge, $V^{t+\Delta t} - V^t$ [mm] is the rainfall variation
 239 by vegetation interception, P_v [mm] is the vegetation interception of rainfall, and E_s



240 [mm] is the actual soil evaporation. The term λ is the evaporation coefficient. The term
241 E_p [mm] is the evaporation capability, which can be measured experimentally or
242 estimated by the water surface evaporation equation E_w . The term F [mm] is the actual
243 soil moisture, F_{sat} [mm] is saturation moisture content, F_c [mm] is field capacity, E_w
244 [mm/d] is evaporation of water surface, and $\Delta e = e_0 - e_{150}$ [hPa] is the draught head
245 between the saturation vapor pressure of the water surface and the air vapor pressure
246 150 m above the water surface (150 m above the water surface was selected here
247 because the altitude for temperature and humidity observations in the southwestern
248 karst regions of China is usually set at 150–200 m). The term $\Delta T = t_0 - T_{150}$ [°C] is the
249 temperature difference between the water surface and the temperature 150 m above the
250 water surface, γ is the relative humidity 150 m above the water surface, and ω [m/s]
251 is the wind speed 150 m above the water surface.

252 3.1.2. Runoff Generation

253 In the QMG model, the surface runoff generation in river channel units means the
254 rainfall in the river system after deducting evaporation losses. This portion of the runoff will
255 participate in the confluence process directly through the river system, rather than
256 undergoing infiltration. In contrast, the process of runoff generation in slope units is more
257 complex, and its classification is related to the developmental characteristics of surface karst
258 in the basin, rainfall intensity, and soil moisture. For example, when the soil moisture
259 content is already saturated, there is the potential for excess infiltration surface runoff in
260 exposed karst slope units. The surface runoff generation of the KHRUs in the river channel
261 units and slope units can be described by the following equations (modified from Chen,
262 2009, 2018; Li et al., 2020):

$$263 \begin{cases} P_r(t) = [P_i(t) - E_p] \frac{L \cdot W_{\text{max}}}{A} \\ R_{\text{sl}} = (P_i - f_i), P_i \geq f_{\text{max}} \\ R_{\text{sl}} = 0, P_i < f_{\text{max}} \\ f_{\text{max}} = \alpha(F_c - F)^\beta + F_s \end{cases} \quad (2)$$

264 Here, $P_r(t)$ [mm] is the net rainfall (deducting evaporation losses) in the river channel
265 units at time t , hours; $P_i(t)$ [mm] is the rainfall in the river channel units, L [m] is the length



266 of the river channel, W_{\max} [m] is the maximum width of the river channel selected, and A
267 [m²] is the cross-sectional area of the river channel. R_{si} is termed excess infiltration runoff in
268 the QMG model, [mm]; when the vadose zone is short of water and has not been filled. The
269 infiltration capacity f_{\max} is different in different karst landform units, α, β are Holtan model's
270 parameters; and F_s [mm] is the stable depth of soil water infiltration.

271 In the KHRUs (Fig. 3), underground runoff is generated primarily from the infiltration
272 of rainwater and direct confluence recharge from sinkholes or skylights. In the QMG model,
273 the underground runoff is calculated by the following equations (modified from Chen,
274 2018):

$$275 \quad \begin{cases} R_g = R_0 \exp(-pt^m) \\ R_e = v_e \cdot I_w \cdot z \end{cases} \quad (3)$$

276 where

$$277 \quad \begin{cases} \frac{\partial R_e}{\partial x} + I_w \cdot z \cdot \frac{\partial F}{\partial t} = R_r - R_{\text{epi}} \\ v_e = K \cdot \tan(\alpha), \quad F > F_c \\ v_e = 0, \quad F \leq F_c \end{cases} \quad (4)$$

278 Here, R_g [mm] is the underground runoff depth (this part of the underground runoff is
279 mainly from the direct confluence supply of the karst sinkholes or skylights in the study
280 area), R_0 [mm] is the average depth of the underground runoff, p and m are attenuation
281 coefficients calculated by conducting a tracer test in the study area, R_e [L/s] is the
282 underground runoff generated from rainfall infiltration in the epikarst zone, I_w [mm] is the
283 width of the underground runoff on the KHRUs, z [mm] is the thickness of the epikarst zone,
284 R_r [mm²/s] is the runoff recharge on the KHRUs during period t , R_{epi} [mm²/s] is the water
285 infiltration from rainfall, v_e [mm/s] is the flow velocity of the underground runoff, K
286 [mm/s] is the current permeability coefficient, and α is the hydraulic gradient of the
287 underground runoff. If the current soil moisture is less than the field capacity, i.e., $F \leq F_c$,
288 then the vadose zone is not yet full, there will be no underground runoff generation, and



289 rainfall infiltration at this time will continue to compensate for the lack of water in the
 290 vadose zone until it is full and before runoff is generated.

291 3.1.3. Channel Routing and Confluence

292 In the QMG model, the calculation of runoff confluence on the KHRUs includes the
 293 confluence of surface river channel and underground runoff. There are already many mature
 294 and classical algorithms available for calculating the runoff confluence in river channel units
 295 and slope units, such as the Saint-Venant equations and Muskingum convergence model. In
 296 this study, the Saint-Venant equations were adopted to describe the confluence in the surface
 297 river and hill slope units, for which a wave movement equation was adopted to calculate
 298 confluence in slope units (Chen, 2009):

$$299 \begin{cases} \frac{\partial Q}{\partial x} + L \frac{\partial h}{\partial t} = q \\ S_f - S_0 = 0 \end{cases} \quad (5)$$

300 where

$$301 Q = v h L = \frac{L}{n} h^{\frac{5}{3}} S_0^{\frac{1}{2}}. \quad (6)$$

302 Here, we customized two variables a and b :

$$303 \begin{cases} a = \left(\frac{n}{L} S_0^{-\frac{1}{2}}\right)^{\frac{3}{5}} \\ b = \frac{3}{5} \end{cases} \quad (7)$$

304 Equation (7) was substituted into equation (5) and discretized by a finite difference
 305 method, giving

$$306 \begin{cases} \frac{\partial Q}{\partial x} + a b Q^{(b-1)} \frac{\partial Q}{\partial t} - q = 0 \\ \frac{\Delta t}{\Delta x} Q_{i+1}^{t+1} + a(Q_{i+1}^{t+1})^b = \frac{\Delta t}{\Delta x} Q_i^{t+1} + a(Q_i^{t+1})^b + q_{i+1}^{t+1} \Delta t \end{cases} \quad (8)$$

307 The Newton–Raphson method was used for the iterative calculation using equation (8):



$$308 \quad [Q_{i+1}^{t+1}]^{k+1} = [Q_{i+1}^{t+1}]^k - \frac{\frac{\Delta t}{\Delta x} [Q_{i+1}^{t+1}]^k + a([Q_{i+1}^{t+1}]^k)^b - \frac{\Delta t}{\Delta x} Q_i^{t+1} - a(Q_{i+1}^t)^b - q_{i+1}^{t+1} \Delta t}{\frac{\Delta t}{\Delta x} + ab([Q_{i+1}^{t+1}]^k)^{b-1}}, \quad (9)$$

309 where Q [L/s] is the confluence of water flow in slope units, L [dm] is its runoff width,
 310 h [dm] is the runoff depth, and q [dm²/s] is the lateral inflow on the KHRUs. Here, the
 311 friction slope S_f equals the hill slope S_0 , and the inertia term and the pressure term in the
 312 motion equation of the Saint-Venant equations were ignored. The term v [dm/s] is the flow
 313 velocity of surface runoff in the slope units as calculated by the Manning equation, n is the
 314 roughness coefficient of the slope units, Q_i^{t+1} [L/s] is the slope inflow in the KHRU at time
 315 $t+1$, and Q_{i+1}^{t+1} [L/s] is the slope discharge in the upper adjacent KHRU at time $t+1$.

316 Similarly, the surface river channel confluence was described based on Saint-Venant
 317 equation, where a diffusion wave movement equation was adopted, means the inertia term in
 318 the motion equation was ignored:

$$319 \quad \begin{cases} \frac{\partial Q}{\partial x} + \frac{\partial A}{\partial t} = q \\ S_f = S_0 - \frac{\partial h}{\partial x} \end{cases} \quad (10)$$

320 A finite difference method and the Newton–Raphson method were used for the iterative
 321 calculation of the above equation:

$$322 \quad \begin{cases} [Q_{i+1}^{t+1}]^{k+1} = [Q_{i+1}^{t+1}]^k - \frac{\frac{\Delta t}{\Delta x} [Q_{i+1}^{t+1}]^k + c([Q_{i+1}^{t+1}]^k)^b - \frac{\Delta t}{\Delta x} Q_i^{t+1} - c(Q_{i+1}^t)^b - q_{i+1}^{t+1} \Delta t}{\frac{\Delta t}{\Delta x} + cb([Q_{i+1}^{t+1}]^k)^{b-1}} \\ c = \left(\frac{1}{3600} n \chi^{\frac{2}{3}} S_f^{-\frac{1}{2}} \right)^{\frac{3}{5}} \end{cases} \quad (11)$$

323 where Q [L/s] is the water flow in surface river channel units, A [dm²] is the discharge
 324 section area, c is a custom intermediate variable, and χ [dm] is the wetted perimeter of the
 325 discharge section area.
 326

327 The underground runoff in the model includes the confluence of epikarst zone and



328 underground river. In the epikarst zone, the karst water-bearing media are highly
329 heterogeneous. For example, the crisscrossed karst fissure systems and conduit systems
330 consisted of large corrosion fractures. When rainfall infiltrates into the epikarst zone, water
331 moves slowly through the small karst fissure systems, while it flows rapidly in larger
332 conduits. The key to determining the confluence velocity lies in the width of karst fractures.
333 In the KHRUs (Fig. 3), the 10-cm width of the fracture was used as a threshold value
334 (Atkinson, 1977), meaning that if the fracture width exceeded 10 cm, then the water
335 movement into it was defined as rapid flow; otherwise, it was defined as slow flow. The
336 confluence in the epikarst zone was calculated by the following equation (modified from
337 Beven and Binley, 2006):

$$338 \quad Q(t)_{ijk} = b_{ijk} \cdot \frac{\Delta h}{\Delta l} R_i C_j \cdot T(t)_{\text{slow/rapid}} \quad (12)$$

339 where

$$340 \quad \begin{cases} T(t)_{\text{slow}} = nr \frac{\rho g R_i C_j L_k}{12\nu} \\ T(t)_{\text{rapid}} = \frac{K_{ij} (e^{-f_{ij} h_{ij}} - e^{-f_{ij} z_{ij}})}{f_{ij}} \end{cases} \quad (13)$$

341 Here, $Q(t)_{ijk}$ [L/s] is the flow confluence in the epikarst zone at time t , b_{ijk} [dm] is
342 the runoff width, $\frac{\Delta h}{\Delta l}$ is the dimensionless hydraulic gradient, $T(t)_{\text{slow/rapid}}$ is the
343 dimensionless hydraulic conductivity, ρ [g/L] is the density of the water flow, g [m/s²] is
344 gravitational acceleration, n is the valid computational units, $R_i C_j L_k$ [L] is the volume of
345 the ijk -th KHRU, ν is kinematic viscosity coefficient, f_{ij} is the attenuation coefficient in
346 the epikarst zone, h_{ij} [dm] is the depth of shallow groundwater, and z_{ij} [dm] is thickness of
347 epikarst zone.

348 The distinction between rapid and slow flows in the epikarst zone is not absolute. The
349 10-cm width of a karst fracture as the dividing threshold also has some subjectivity. In fact,
350 there is usually water exchange between the rapid and slow flows at the junction of large and
351 small fissures in karst aquifers. In the QMG model, this water exchange can be described



352 with this equation (modified form Li et al., 2021):

$$353 \quad \begin{cases} Q = \alpha_{i,j,k} (h_n - h_{i,j,k}) \\ \alpha_{i,j,k} = \sum_{ip=1}^{np} \frac{(K_w)_{i,j,k} \pi d_{ip} \frac{1}{2} (\Delta l_{ip} \tau_{ip})}{r_{ip}} \end{cases} \quad (14)$$

354 Here, $\alpha_{i,j,k}$ [dm²/s] is the water exchange coefficient in the ijk -th KHRU,
 355 $(h_n - h_{i,j,k})$ [dm] is the water head difference between the rapid and slow flows at the
 356 junction of large and small fissures in KHRUs, np is the number of fissure systems
 357 connected to the adjacent conduit systems, $(K_w)_{i,j,k}$ [dm/s] is the permeability coefficient
 358 at the junction of a fissure and conduit, d_{ip} and r_{ip} [dm] are the conduit diameter and
 359 radius, respectively, Δl_{ip} [dm] is the length of the connection between conduits i and p , and
 360 τ_{ip} is the conduit curvature. Some of the parameters in this equation, such as $(K_w)_{i,j,k}$
 361 and $(h_n - h_{i,j,k})$, were obtained by conducting an infiltration test in the study area.

362 The confluence of the underground river system plays an important role for the
 363 confluence at the basin outlet. To facilitate the calculation of confluence in the QMG model,
 364 the underground river systems can be generalized into large multiple conduit systems.
 365 During floods, these conduit systems are mostly under pressure. Whether the water flow is
 366 laminar or turbulent depends on the flow regime at that time. The water flow into these
 367 conduits is calculated by the Hagen–Poiseuille equation and the Darcy–Weisbach equation
 368 (Shoemaker et al., 2008):

$$369 \quad \begin{cases} Q_{\text{laminar}} = -A \frac{gd^2 \partial h}{32\nu \partial x} = -A \frac{\rho g d^2 \Delta h}{32\mu \tau \Delta l} \\ Q_{\text{turbulent}} = -2A \sqrt{\frac{2gd|\Delta h|}{\Delta \tau}} \log \left(\frac{H_c}{3.71d} + \frac{2.51\nu}{d \sqrt{\frac{2gd^3|\Delta h|}{\Delta \tau}}} \right) \frac{\Delta h}{|\Delta h|} \end{cases} \quad (15)$$

370 Here, Q_{laminar} [L/s] is the water flow of the laminar flow in the conduit systems, A



371 [dm²] is the conduit cross-sectional area, d [dm] is the conduit diameter, ρ [kg/dm³] is the
372 density of the underground river, $\nu = \mu / \rho$ is the coefficient of kinematic viscosity,
373 $\Delta h / \tau \Delta l$ is the hydraulic slope of the conduits, τ is the dimensionless conduit curvature,
374 $Q_{\text{turbulent}}$ [L/s] is the turbulent flow in the conduit systems, and H_c [dm] is the average
375 conduit wall height.

376 3.2. Parameter Optimization

377 In total, the QMG model has 12 parameters, of which flow direction and slope are
378 topographic parameters that can be determined from the DEM without parametric
379 optimization, while the remaining 10 parameters require calibration. Other distributed
380 hydrological models with multiple structures usually have many parameters. For example,
381 the Karst-Liuxihe model (Li et al., 2021) has 15 parameters that need to be calibrated. In the
382 QMG model, each parameter is normalized as

$$383 \quad x_i = x_i^* / x_{i0}, \quad (16)$$

384 where x_i is the dimensionless parameter value i after it is normalized, x_i^* is the
385 parameter value i with an actual physical property, and x_{i0} is the initial or final value of x_i .
386 Through the processing of equation (16), the value range of the model parameters is limited to
387 a hypercube $K_n = (X \mid 0 \leq x_i \leq 1, i = 1, 2, \dots, n)$, which is a dimensionless value. Such a
388 normalized treatment can ignore the influence of the spatiotemporal variation of the
389 underlying surface attributes on the parameters and at the same time simplify the parameter
390 classification and parameter number of the model to a certain extent. Accordingly, the model
391 parameters can be further divided into rainfall-evaporation parameters, epikarst-zone
392 parameters, and underground-river parameters. Table 1 lists the parameters of the QMG
393 model.

394 Table 1 Parameters of QMG model.

395 Because the QMG model has relatively few parameters, it is possible to calibrate
396 them manually, which has the advantage that the operation is easy to implement and does
397 not require a special program for parameter optimization. However, the disadvantage is that



398 it is subjective, which can lead to great uncertainty in the manual parameter calibration
399 process. To compare the effects of parameter optimization on model performance, this study
400 used both a manual calibration of parameters and the improved chaotic particle swarm
401 algorithm (IPSO) for the automatic calibration of model parameters, and compared the
402 effects of both on flood simulation.

403 In general, the structure and parameters of a standard particle swarm algorithm
404 (PSO) are simple, with the initial parameter values obtained at random. For parameter
405 optimization in high-dimensional, multi-peak hydrological models, the standard PSO is
406 easily limited to a local convergence and cannot achieve the optimal effect, while the late
407 evolution of the algorithm may also cause problems, such as precocity and stagnant
408 evolution, due to the “inert” aggregation of particles, which seriously affects the efficiency
409 of parameter selection. It is necessary to overcome the above problems and make the
410 algorithm converge to the global optimal solution with a high probability. In parameter
411 optimization for the QMG model, we improved the standard PSO algorithm by adding chaos
412 theory, and developed the IPSO, where 10 cycles of chaotic disturbances were added to
413 improve the activity of the particles. The inverse mapping equation of the chaotic variable is
414 as follows:

$$415 \begin{cases} X_{ij} = X_{\min} + (X_{\max} - X_{\min}) * Z_{ij} \\ Z'_{ij} = (1 - \alpha)Z^* + \alpha Z_{ij} \end{cases} \quad (17)$$

416 where X_{ij} is the optimization variable for the model parameters, $(X_{\max} - X_{\min})$ is the
417 difference between its maximum and its minimum, Z_{ij} is the variable before the disturbance is
418 added, and Z'_{ij} represents the chaotic variables after a disturbance is added, α is a variable
419 determined by the adaptive algorithm, $0 \leq \alpha \leq 1$, and Z^* is the chaotic variable formed when
420 the optimal particle maps to the interval [0,1]. In parameter optimization, the flowchart of the
421 IPSO is shown in Fig. 4.

422 Figure 4 Algorithm flow chart of the IPSO.



423 3.3. Uncertainty Analysis

424 As a type of mathematical and physical model, a hydrological model has some
425 uncertainty in flood simulation and forecasting because of the errors in system structure and
426 the algorithm (Krzysztofowicz and Kelly, 2000). A multi-parametric sensitivity analysis
427 method (Choi et al., 1999; Li et al., 2020) was used to analyze the sensitivity of the
428 parameters in the QMG model. Parameter sensitivity analysis steps are as follows.

429 1) Selection of appropriate objective function

430 The Nash–Sutcliffe coefficient is widely used as the objective function to evaluate the
431 performance of hydrological models (Li et al., 2020, 2021). It was therefore used to assess
432 the QMG model. Because the most important factor in flood forecasting is the peak
433 discharge, it is used in the Nash coefficient equation:

$$434 \quad NSC = 1 - \frac{\sum_{i=1}^n (Q_i - Q_i')^2}{\sum_{i=1}^n (Q_i - \bar{Q})^2}, \quad (18)$$

435 where NSC is Nash–Sutcliffe coefficient values, Q_i [L/s] is the observed flow discharges, Q_i'
436 [L/s] is the simulated discharge, \bar{Q} [L/s] is the average value of the observed discharges,
437 and n [h] is the observation period.

438 2) Parameter sequence sampling

439 The Monte Carlo sampling method was applied to sample 8,000 groups of parameter
440 sequences. The parametric sensitivity of the QMG model was analyzed and evaluated by
441 comparing the differences between the a priori and a posteriori distributions of the
442 parameters.

443 3) Parameter sensitivity assessment

444 The a priori distribution means its probability distribution of a model parameter, while
445 the a posteriori distribution can be calculated based on the simulation result of the
446 parametric optimization. If there is a significant difference between them, then the parameter
447 being tested has a high sensitivity, whereas if there is no obvious difference, then the
448 parameter is insensitive. The parametric priori distribution is calculated as follows:



$$\left\{ \begin{array}{l} P_{i,j}(NSC_{i,j} \geq 0.85) = \frac{n}{N+1} \times 100 \\ \sigma_i = \sum_{j=1}^n (P_{i,j} - \overline{P_{i,j}})^2 \end{array} \right. \quad (19)$$

449 where $P_{i,j}$ is the priori distribution'probability when $NSC_{i,j} \geq 0.85$. We used a
450 simulated Nash coefficient of 0.85 as the threshold value, and n was the number of
451 occurrences of a Nash coefficient greater than 0.85 in flood simulations. In each simulation,
452 only a certain parameter was changed, while the remaining parameters remained unchanged.
453 If the Nash coefficient of this simulation exceeded 0.85, then the flood simulation results
454 were considered acceptable. The term σ_i is the difference between the acceptable value
455 and its mean, which represents the parametric sensitivity ($0 < \sigma_i < 1$). The higher the σ_i
456 value, the more sensitive the parameter. N is the 8,000 parameter sequences, and $\overline{P_{i,j}}$ is the
457 average value of the a priori distribution.
458

459 3.4. Model Setting

460 Once the model was built, some of the initial conditions had to be set before running it
461 to simulate and forecast floods, such as basin division, the setting of initial soil moisture, and
462 the assumption of the initial parameter range. 1) In the study area, the entire Qingmuguan
463 karst basin was divided into 893 KHRUs, including 65 surface river units, 466 hill slope
464 units, and 362 underground river units. The division of these units formed the basis for
465 calculating the process of runoff generation and convergence. 2) The initial soil moisture
466 was set to 0–100% of the saturation moisture content in the basin, and the specific soil
467 moisture before each flood had to be determined by a trial calculation. 3) The waterhead
468 boundary conditions of the groundwater were determined by a tracer test in the basin, where
469 a perennial stable water level adjacent the groundwater-divide was used as the fixed
470 waterhead boundary. The base flow of the underground river was determined to be 35 L/s
471 from the perennial average dry season runoff. 4) The range of initial parameters and
472 convergence conditions were assumed before parameter optimization (Figure 4). 5)
473 Parameter optimization and flood simulation validated the performance of the QMG model



474 in karst basins.

475 **4. Results and Discussion**

476 **4.1. Parameter Sensitivity Results**

477 The number of parameters in a distributed hydrological model is generally large, and it
478 is important to perform a sensitivity analysis of each parameter to quantitatively assess the
479 impact of the different parameters on model performance. In the QMG model, each
480 parameter was divided into four categories according to its sensitivity: (i) highly sensitive,
481 (ii) sensitive, (iii) moderately sensitive, and (v) insensitive. In the calibration of model
482 parameters, insensitive ones do not need to be calibrated, which can greatly reduce the
483 amount of calculation and improve the efficiency of model operation.

484 The flow process in the calibration period (14 April to 10 May 2017) was adopted to
485 calculate the sensitivity of the model parameters, for which the calculation principle was
486 equation (19), and the parameter sensitivity results are calculated in Table 2.

487 Table 2 Parametric sensitivity results in QMG model.

488 In Table 2, the value of σ_i [equation (19)] represents a parameter's sensitivity, and the
489 higher the value, the more sensitive the parameter is. From the results in Table 2, it was
490 found that the rainfall infiltration coefficient, rock permeability coefficient, rock porosity,
491 and the related parameters of soil water content, such as the saturated water content, and
492 field capacity, were sensitive parameters. The order of parameter sensitivity was as follows:
493 infiltration coefficient > permeability coefficient > rock porosity > specific yield > saturated
494 water content > field capacity > flow direction > thickness > slope > Soil coefficient >
495 channel roughness > evaporation coefficient.

496 In the QMG model, parameters are classified as highly sensitive, sensitive, moderately
497 sensitive, and insensitive according to their influence on the flood simulation results. In
498 Table 4, we divided the sensitivity of model parameters into four levels based on the σ_i
499 value: 1) highly sensitive parameters, $0.8 < \sigma_i < 1$; 2) sensitive parameters, $0.65 < \sigma_i < 0.8$;



500 3) moderately sensitive parameters, $0.45 < \sigma_i < 0.65$; and 4) insensitive parameters,
501 $0 < \sigma_i < 0.45$. The highly sensitive parameters were the infiltration coefficient, permeability
502 coefficient, rock porosity, and specific yield. The sensitive parameters were the saturated
503 water content, field capacity, and thickness of the epikarst zone. The moderately sensitive
504 parameters were flow direction, slope, and soil coefficient. The insensitive parameters were
505 channel roughness and the evaporation coefficient.

506 4.2. Parametric Optimization

507 In total, the QMG model has 12 parameters, of which only eight need to be optimized,
508 which is relatively few for distributed models. The parameters of flow direction and slope as
509 well as the insensitive parameters of channel roughness and the evaporation coefficient need
510 not be calibrated, which can improve the convergence efficiency of the model parameter
511 optimization.

512 In the study area, 18 karst floods during the period of 14 April 2017 to 10 June 2019
513 were recorded at underground river outlet to validate the effects of the QMG model in karst
514 hydrological simulations. The calibration period was 14 April to 10 May 2017 at the
515 beginning of the flow process, with the remainder of the time being the validation period. In
516 the QMG model, the IPSO algorithm was used to optimize the model parameters. To show
517 the necessity of parameter optimization for the distributed hydrological model, the study
518 specifically compared the flood simulations obtained using the initial parameters of the
519 model (without parameter calibration) and the optimized parameters. Fig. 5 shows the
520 iteration process of parameter optimization for the QMG model.

521 Figure 5 Iteration process of parametric optimization.

522 Fig. 5 shows that almost all parameters fluctuated widely at the beginning of the
523 optimization, and then after about 15 iterations of the optimization calculation, most of the
524 linear fluctuations become significantly less volatile, which indicated that the algorithm
525 tended to converge (possibly only locally). When the number of iterations exceeded 25, all
526 parameters remained essentially unchanged, meaning that the algorithm had converged (at
527 this point there was global convergence). It took only 25 iterations to reach a definite



528 convergence of the parameter rates with this IPSO algorithm, which is extremely efficient in
529 terms of the parameter optimization of distributed hydrological models. In previous studies
530 of the parametric optimization for the Karst-Liuxihe model in similar basin areas, 50
531 automatic parameter optimization iterations were required to reach convergence (Li et al.,
532 2021), demonstrating the effectiveness of the IPSO algorithm.

533 To evaluate the effect of parameter optimization, the convergence efficiency of the
534 algorithm, and more importantly, the parameters after calibration were used to simulate
535 floods. Fig. 6 shows the flood simulation effects.

536 Figure 6 Flow simulation results of QMG model based on parameter optimization.

537 Fig. 6 shows that the flows simulated by parameter optimization were better than those
538 simulated by the initial model parameters. The simulated flow processes based on the initial
539 parameters were relatively small, with the simulated peak flows in particular being smaller
540 than the observed values, and there were large errors between the two values. In contrast, the
541 simulated flows produced by the QMG model after parameter optimization were very
542 similar to the observed values, which indicates that calibration of the model parameters is
543 necessary and that there was an improvement in parameter optimization through the use of
544 the IPSO algorithm in this study. In addition, it was found that the flow simulation effect
545 was better in the calibration periods than in the validation periods (Fig. 6).

546 To compare the results of the flow processes simulation with the initial model
547 parameters and the optimized parameters, six evaluation indices (Nash–Sutcliffe coefficient,
548 correlation coefficient, relative flow process error, flood peak error, water balance
549 coefficient, and peak time error) were applied in this study, and the results are presented in
550 Table 3.

551 Table 3 Flood simulation evaluation index through parametric optimization.

552 Table 3 shows that the evaluation indices of the flood simulations after parametric
553 optimization were better than those of the initial model parameters. The average values of
554 the initial parameters for these six indices 0.81, 0.74, 27%, 31%, 0.80, and 5 h, respectively.
555 For the optimized parameters, the average values were 0.90, 0.91, 16%, 14%, 0.94, and 3 h,



556 respectively. The flood simulation effects after parameter optimization clearly improved,
557 implying that parameter optimization for the QMG model is necessary, and the IPSO
558 algorithm for parameter optimization is an effective approach that can greatly improve the
559 convergence efficiency of parameter optimization, and also ensure that the model performs
560 well in flood simulations.

561 **4.3. Model Validation in Flood Simulations**

562 Following parameter optimization, we simulated the whole flow process (14 April 2017
563 to 10 June 2019) based on the optimized and initial parameters of the QMG model (Fig. 6),
564 which enabled a visual reflection of the model used in the simulation of a long series of flow
565 processes. To reflect the simulation effect of the model for different flood events, we divided
566 the whole flow process into 18 flood events, then used the initial parameters of the model
567 and the optimized parameters, respectively, to verify the model performance in flood
568 simulations. Fig. 7 and Table 4 show the flood simulation effects and their evaluation indices
569 using both the initial and the optimized parameters.

570 Figure 7 Flood simulation effects based on initial and optimized parameters.

571 Table 4 Flood simulation indices for model validation.

572 Fig. 7 shows that the flood simulation results using the initial parameters were smaller
573 than the observed values, and the model performance improved in flood simulations after
574 parameter optimization. The simulated flood processes were in good agreement with
575 observations, and were especially effective for simulating flood peak flows. From flood
576 simulation indices in Table 4, the average water balance coefficient based on the initial
577 parameters was 0.69, i.e., much less than 1, indicating that the simulated water in the model
578 was unbalanced. After parameter optimization, the average value was 0.92, indicating that
579 parameter optimization had a significant impact on the model water balance calculation.

580 Table 4 shows that the average values of the six indices (Nash–Sutcliffe coefficient,
581 correlation coefficient, relative flow process error, flood peak error, water balance
582 coefficient, and peak time error) for the initial parameters were 0.79, 0.74, 26%, 25%, 0.69,
583 and 5 h, respectively, while for the optimized parameters the average values were 0.92, 0.90,



584 10%, 11%, 0.92, and 2 h, respectively. All evaluation indices improved after parameter
585 optimization, with the average values of the Nash coefficient, correlation coefficient, and
586 water balance coefficient increasing by 0.13, 0.16, and 0.23, respectively. The average
587 values of the relative flow process error, flood peak error, and peak time error decreased by
588 15%, 14%, and 3 h, respectively. These reasonable flood simulation results confirmed that
589 parameter optimization by the IPSO algorithm was necessary and effective for the QMG
590 model.

591 Compared with the overall flow process simulation shown in Figure 6, each flood
592 process was better simulated by the QMG model (Fig. 7). This was because in the function
593 of the QMG model and its algorithm design, the main consideration was the calculation of
594 the flood process, but the correlation algorithm of the dry season runoff was not described
595 well enough. For example, equations (12)–(15) are the flood convergence algorithm. As a
596 result, the model is not good at simulating other flow processes, such as dry season runoff,
597 leading to a low accuracy in the overall flow process. The next phase of our research will
598 focus on refining the algorithm related to dry season runoff and improving the
599 comprehensive performance of the model.

600 **4.4. Uncertainty Analysis**

601 **4.4.1 Assessment and Reduction of Uncertainty**

602 In general, the uncertainty in model simulations are mainly derived from three aspects
603 of the model: 1) the uncertainty of the model input data, 2) the uncertainty of model
604 structure and the algorithm, and 3) the uncertainty of model parameters. In the practical
605 application of a hydrological model, these three uncertainties are usually interwoven, which
606 leads to the overall uncertainty of the final simulation results (Krzysztofowicz, 2014).
607 Therefore, this study focused on the input data, the model structure, and parameter
608 uncertainty to reduce the overall uncertainty of simulation results.

609 First, the input data (e.g., rainfall, flood event, and some hydrogeological data) were
610 validated and pre-processed through observations in this study, which substantially reduced
611 the uncertainty.



612 Second, we simplified the structure of the QMG model. The model was designed with
613 full consideration of the relationship between the amount of data required to build the model
614 and its performance for flood simulation and forecasting in karst regions, and the model's
615 entire framework was integrated through simple structures and easy-to-implement
616 algorithms, using the concept of distributed hydrological modeling. Conventionally, the
617 extent of uncertainty is increased with the growing complexity of the model structure. We
618 therefore ensured that the structure of the QMG model was simple when it was designed,
619 and the model was divided into surface and underground double layer structures. Such a
620 relatively simple structure made the uncertainty of the model structure reduced largely. In
621 contrast, the underground structure of our previous Karst-Liuxihe model (Li et al., 2021) has
622 five layers, which leads to great uncertainty.

623 Third, appropriate algorithms for runoff generation and confluence were selected. The
624 design function of different models is different, which leads to great differences in the
625 algorithms used. In the QMG model, most of the rainfall-runoff algorithms used have been
626 validated by the research results of others, and some of them were improved to suit karst
627 flood simulation and forecasting by the QMG model. For example, the algorithm of excess
628 infiltration runoff generation [equation (2)] was an improvement of the version used in the
629 Liuxihe model (Chen, 2009, 2018; Li et al., 2020).

630 Finally, the algorithm of parameter optimization was improved. Considering the
631 shortcomings of the standard PSO algorithm that tends to reach a local convergence, this
632 study developed the IPSO for parameter optimization by adding chaotic perturbation factors.
633 The flood simulation results after parameter optimization were much better than those of the
634 initial model parameters (Figs. 6 and 7 and Tables 2 and 3), which indicates that parameter
635 optimization is necessary for a distributed hydrological model and can reduce the
636 uncertainty of model parameters.

637 **4.4.2 Parameter Sensitivity Analysis**

638 From the results of parameter sensitivity in Table 2, it can be seen that the rainfall
639 infiltration coefficient in the QMG model was the most sensitive parameter. It was the key to



640 determining the generation of excess infiltration surface runoff and dividing surface runoff
641 from subsurface runoff. If the rainfall infiltration coefficient was greater than the infiltration
642 capacity, it would generate excess infiltration surface runoff on the exposed karst landforms;
643 otherwise, all rainfall would infiltrate to meet the water deficit in the vadose zone, and then
644 continue to seep down into the underground river system, eventually flowing out of the basin
645 through the underground river outlet. The confluence modes of surface runoff and
646 underground runoff were completely different, resulting in a large difference in the
647 simulated flow results. Therefore, the rainfall infiltration coefficient had the greatest impact
648 on the final flood simulation results.

649 Other highly sensitive parameters such as the rock permeability coefficient, rock
650 porosity, and specific yield were used as the basis for the division of slow flow in karst
651 fissures and rapid flow in conduits. The division of slow and rapid flows also had a great
652 impact on the discharge at the outlet of the basin. Slow flow plays an important role in water
653 storage in a karst aquifer and is very important for the replenishment of river base flow in
654 the dry season. Rapid flow in large conduit systems dominates of the flood runoff and is the
655 main component of the flood water volume in the flood season.

656 Parameters related to the soil water content, including the saturated water content, field
657 capacity, and thickness, were sensitive parameters and had a large influence on the flood
658 simulation results. This is because the soil moisture content prior to flooding affects how
659 flood flows rise and when peaks occur. If the soil is already very wet or even saturated
660 before the flooding, the flood will quickly rise to reach a peak, and the process line of the
661 flood peak flow will be sharp and thin. This type of flood process forms easily and can lead
662 to disaster-causing flood events. In contrast, if the soil in the basin is very dry before the
663 flooding, the rainfall will first meet the water shortage of the vadose zone, and after it is
664 replenished the rainfall will infiltrate into the underground river. The flood peak of the river
665 basin outlet is therefore delayed.

666 The moderately sensitive parameters were flow direction, slope, and the soil coefficient.
667 They had a specific influence on the flood simulation results, but the influence was not as
668 great as the highly sensitive and sensitive parameters. The insensitive parameters were



669 channel roughness and the evaporation coefficient. The amount of water lost by
670 evapotranspiration is very small in the total flood water, and it was therefore the least
671 sensitive parameter in the QMG model.

672 **5. Conclusions**

673 This study proposed a new distributed physically based hydrological model, i.e., the
674 QMG model, to simulate floods accurately in karst trough valley. The main conclusions of
675 this paper are as follows.

676 This QMG model has a high application potential in karst hydrology simulations. Other
677 distributed hydrological models usually have multiple structures, resulting in the need for a
678 large amount of data to build models in karst areas (Kraller et al., 2014). The QMG model
679 has only a double-layer structure, with a clear physical meaning, and a small amount of
680 basic data is needed to build the model in karst areas, such as some necessary
681 hydrogeological data. For example, the distribution and flow direction of underground rivers
682 is required, which can be inferred from a tracer test, leading to a low modeling cost. There
683 were fewer parameters in the QMG model than in other distributed hydrological models,
684 with only 10 parameters that needed to be calibrated.

685 The flood simulation after parameter optimization was much better than the simulation
686 using the initial model parameters. After parameter optimization, the average value of Nash
687 coefficient, correlation coefficient, and water balance coefficient increased by 0.13, 0.16,
688 and 0.23, respectively; while the average relative flow process error, flood peak error, and
689 peak time error decreased by 15%, 14%, and 3 h, respectively. Parameter optimization is
690 necessary for a distributed hydrological model, and the improvement of the IPSO algorithm
691 in this study was an effective way to achieve this.

692 In the QMG model, the rainfall infiltration coefficient, I_c , rock permeability coefficient,
693 K , rock porosity, R_p , and the parameters related to the soil water content were sensitive
694 parameters. The order of parameter sensitivity was: infiltration coefficient > permeability
695 coefficient > rock porosity > specific yield > saturated water content > field capacity > flow
696 direction > thickness > slope > soil coefficient > channel roughness > evaporation



697 coefficient.

698 This QMG model is suitable for karst trough valley basins, where the topography is
699 conducive to the spread of flood water. Whether this model is applicable to other karst areas
700 in non-trough valley regions still needs to be verified in the future studies. In addition, the
701 basin area is very small, where the hydrological similarity between different small basin
702 areas varies greatly (Kong and Rui, 2003). The size of the area to be modeled has a great
703 influence on the choice of model spatial resolution (Chen et al., 2017). Therefore, whether
704 the QMG model is suitable for flood forecasting in large karst basins needs to be
705 determined.

706 **Model development.**

707 This QMG model presented in this study uses the Visual Basic language programming. The
708 general framework of the model and the algorithm consist of three parts: the modeling
709 approach, the algorithm of rainfall-runoff generation and confluence, and the parameter
710 optimization algorithm. As a free and open source hydrological modeling program (QMG
711 model-V1.0), we provide all modeling packages, including model code, installation package,
712 simulation data package and user manual, free of charge. It is important to note that the
713 model we provide are for scientific research purposes only and should not be used for any
714 commercial purposes. Creative Commons Attribution 4.0 International.

715 Model installation program can be downloaded from ZENODO, cite as JI LI. (2021, June
716 16). QMG model-V1.0. Zenodo. <http://doi.org/10.5281/zenodo.4964701>, and
717 <http://doi.org/10.5281/zenodo.4964697> (registration required). User manual can be
718 downloaded from <http://doi.org/10.5281/zenodo.4964754>.

719 **Code availability.**

720 All code for the QMG model-V1.0 in this paper are available and free, the code can be
721 downloaded from ZENODO, Cite as JI LI. (2021, June 16). QMG model-V1.0 code
722 (Version v1.0). Zenodo. <http://doi.org/10.5281/zenodo.4964709> (registration required).

723 **Data availability.**

724 All data used in this paper are available, findable, accessible, interoperable, and reusable.
725 The simulation data and modelling data package can be downloaded from
726 <http://doi.org/10.5281/zenodo.4964727>. The DEM was downloaded from the Shuttle Radar
727 Topography Mission database at <http://srtm.csi.cgiar.org>. The land use-type data were
728 downloaded from <http://landcover.usgs.gov>, and the soil-type data were downloaded from
729 <http://www.isric.org>. These data were last accessed on 15 October 2020.

730 **Author contributions.** JIL was responsible for the calculations and writing of the whole



731 paper. DY and YJ helped conceive the structure of the model. ZF and JL provided significant
732 assistance in the English translation of the paper. MM provided flow data of the study area.

733 **Competing interests.**

734 The authors declare that they have no conflicts of interest.

735 **Acknowledgments.**

736 This study was supported by the National Natural Science Foundation of China (41830648),
737 Chongqing Municipal Science and Technology Commission Fellowship Fund
738 (cstc2019sysz-jcyjX0002), and the drought monitoring, analysing and early warning of
739 typical prone-to-drought areas of Chongqing (20C00183).



740 **References**

- 741 Abbott, M. B., Bathurst, J. C., Cunge, J. A., O’Connell, P. E., and Rasmussen, J.: An
742 Introduction to the European Hydrologic System-System Hydrologue Europeen, ‘SHE’,
743 a: History and Philosophy of a Physically-based, Distributed Modelling System, J.
744 Hydrol., 87, 45–59, 1986a.
- 745 Abbott, M. B., Bathurst, J. C., Cunge, J. A., O’Connell, P. E., and Rasmussen, J.: An
746 Introduction to the European Hydrologic System-System Hydrologue Europeen, ‘SHE’,
747 b: Structure of a Physically based, distributed modeling System, J. Hydrol., 87, 61–77,
748 1986b.
- 749 Ambrose, B., Beven, K., and Freer, J.: Toward a generalization of the TOPMODEL
750 concepts: Topographic indices of hydrologic similarity. Water Resources Research, 32,
751 2135-2145, 1996.
- 752 Atkinson, T.C.: Diffuse flow and conduit flow in limestone terrain in the Mendip Hills,
753 Somerset (Great Britain). Journal of Hydrology, 35, 93-110.
754 [https://doi.org/10.1016/0022-1694\(77\)90079-8](https://doi.org/10.1016/0022-1694(77)90079-8), 1977.
- 755 Berry, R.A., Saurel, R., and Lemetayer, O.: The discrete equation method (DEM) for fully
756 compressible, two-phase flows in ducts of spatially varying cross-section. Nuclear
757 Engineering & Design, 240(11), 3797-3818, 2010.
- 758 Beven, K., and Binley, A.: The future of distributed models: Model calibration and
759 uncertainty prediction. Hydrological Processes, 6, 279-298, 2006.
- 760 Birk, S., Geyer, T., Liedl, R., and Sauter, M.: Process-based interpretation of tracer tests in
761 carbonate aquifers. Ground Water, 43(3), 381-388, 2005.
- 762 Bittner, D., Parente, M.T., Mattis, S., Wohlmuth, B., and Chiogna, G.: Identifying relevant
763 hydrological and catchment properties in active subspaces: An inference study of a
764 lumped karst aquifer model. ADVANCES IN WATER RESOURCES, 135, 550-560.
765 [doi: 10.1016/j.advwatres.2019.103472](https://doi.org/10.1016/j.advwatres.2019.103472), 2020.



- 766 Blansett, K. L., and Hamlett, J. M.: Challenges of Stormwater Modeling for Urbanized Karst
767 Basins. Pittsburgh, Pennsylvania, an ASABE Meeting Presentation, Paper Number:
768 1009274. doi:10.13031/2013.29840, 2010.
- 769 Blansett, K. L.: Flow, water quality, and SWMM model analysis for five urban karst basins..
770 (Doctoral dissertation). The Pennsylvania State University, USA, 2011.
- 771 Chang, Y., and Liu, L.: A review of hydrological models in karst areas. Engineering
772 investigation, 43,37-44, 2015.
- 773 Chen, G.M., Jia, J.Y., and Han, Q.: Research on inertia weight reduction strategy of Particle
774 Swarm optimization algorithm. Journal of Xi'an Jiaotong University, 40(1),53-56, 2006.
- 775 Choi, J., Harvey, J. W., and Conklin, M. H.: Use of multi-parameter sensitivity analysis to
776 determine relative importance of factors influencing natural attenuation of mining
777 contaminants. the Toxic Substances Hydrology Program Meeting, Charleston, South
778 Carolina, 1999.
- 779 Chen, Y. B.: Liuxihe Model, China Science and Technology Press, Beijing, China, 2009.
- 780 Chen, Y., Li, J., and Xu, H.: Improving flood forecasting capability of physically based
781 distributed hydrological models by parameter optimization. Hydrol. Earth Syst. Sci. 20,
782 375-392. <https://doi.org/10.5194/hess-20-375-2016>, 2016.
- 783 Chen, Y., Li, J., Wang, H., Qin, J., and Dong, L.: Large watershed flood forecasting with
784 high-resolution distributed hydrological model. Hydrol. Earth Syst. Sci. 21, 735-749.
785 <https://doi.org/10.5194/hess-21-735-2017>, 2017.
- 786 Chen, Y.: Distributed Hydrological Models. Springer Berlin Heidelberg, Berlin, Germany.
787 https://doi.org/10.1007/978-3-642-40457-3_23-1, 2018.
- 788 Dewandel, B., Lachassagne, P., Bakalowicz, M., Weng, P., and Malki, A.A.: Evaluation of
789 aquifer thickness by analysing recession hydrographs. Application to the Oman
790 ophiolite hard-rock aquifer. Journal of Hydrology, 274,248-269, 2003.
- 791 Dubois, E., Doummar, J., Séverin Pistre, S., and Larocque, M.: Calibration of a lumped karst
792 system model and application to the Qachqouch karst spring (Lebanon) under climate



- 793 change conditions. Hydrol. Earth Syst. Sci., 24, 4275-4290.
794 <https://doi.org/10.5194/hess-24-4275-2020>, 2020.
- 795 Doummar, J., Sauter, M., and Geyer, T.: Simulation of flow processes in a large scale karst
796 system with an integrated catchment model (MIKE SHE) – identification of relevant
797 parameters influencing spring discharge. Journal of Hydrology, 426-427, 112-123,
798 2012.
- 799 Epting, J., Page, R.M., and Auckenthaler, A.: Process-based monitoring and modeling of
800 Karst springs–Linking intrinsic to specific vulnerability. Science of the Total
801 Environment, 625, 403-415, 2018.
- 802 Fleury, P., Plagnes, V., and Bakalowicz, M.: Modelling of the functioning of karst aquifers
803 with a reservoir model: Application to Fontaine de Vaucluse (South of France). Journal
804 of Hydrology, 345,38-49. <http://dx.doi.org/10.1016/j.jhydrol.2007.07.014>, 2007b.
- 805 Ford, D. C., and Williams, P.W.: Karst geomorphology and hydrology. Wiley, Chichester,
806 England, 2007.
- 807 Gang, L., Tong, F.G., and Bin,T.: A Finite Element Model for Simulating Surface Runoff and
808 Unsaturated Seepage Flow in the Shallow Subsurface. Hydrological Processes,
809 6,102-120. doi: 10.1002/hyp.13564, 2019.
- 810 Geyer, T., Birk, S., Liedl, R., and Sauter, M.: Quantification of temporal distribution of
811 recharge in karst systems from spring hydrographs. Journal of Hydrology, 348(30),
812 452-463, 2008.
- 813 Gou, P.F., Jiang, Y.J., Hu, Z.Y., Pu, J.B., and Yang, P.H.: A study of the variations in
814 hydrology and hydrochemistry under the condition of a storm in a typical karst
815 subterranean stream. HYDROGEOLOGY&ENGINEERING GEOLOGY,37(5),20-25,
816 2010.
- 817 Hartmann, A., and Baker, A.: Progress in the hydrologic simulation of time variant of karst
818 systems-Exemplified at a karst spring in Southern Spain. Advances in Water Resources,
819 54,149-160, 2013.



- 820 Hartmann, A., Goldscheider, N., Wagener, T., Lange, J., and Weiler, M.: Karst water
821 resources in a changing world: Review of hydrological modeling approaches. *Reviews*
822 *of Geophysics* 52: 218-242. doi: [10.1002/2013RG000443](https://doi.org/10.1002/2013RG000443), 2014a.
- 823 Hartmann, A., and Baker, A.: Modelling karst vadose zone hydrology and its relevance for
824 paleoclimate reconstruction. *Earth-Science Reviews*, 172, 178-192, 2017.
- 825 Hartmann, A.: Experiences in calibrating and evaluating lumped karst hydrological models.
826 London: Geological Society, Special Publications, 2018.
- 827 Jukić, D., and Denić-Jukić, V.: Groundwater balance estimation in karst by using a
828 conceptual rainfall–runoff model. *Journal of Hydrology*, 373, 302-315.
829 <http://dx.doi.org/10.1016/j.jhydrol.2009.04.035>, 2009.
- 830 Kong, F.Z., and Rui, X.F.: Hydrological similarity of catchments based on topography.
831 *GEOGRAPHICAL RESEARCH*, (06), 709-715, 2003.
- 832 Kovács, A., and Sauter, M.: Modelling karst hydrodynamics. In: Goldscheider N, Drew D
833 (eds) *Methods in karst hydrogeology*, IAH international contributions to hydrogeology;
834 26,264 p, 2007.
- 835 Kovács, A., and Perrochet, P.: A quantitative approach to spring hydrograph decomposition.
836 *Journal of Hydrology*, 352, 16-29. <http://dx.doi.org/10.1016/j.jhydrol.2007.12.009>,
837 2008.
- 838 Kurtulus, B., and Razack, M.: Evaluation of the ability of an artificial neural network model
839 to simulate the input-output responses of a large karstic aquifer: the la rochefoucauld
840 aquifer (charente, france). *Hydrogeology Journal*, 15(2), 241-254, 2007.
- 841 Krzysztofowicz, R., and Kelly, K.: Hydrologic uncertainty processor for probabilistic river
842 stage forecasting. *Water Resources Research*, 36(11),3265-3277, 2000.
- 843 Krzysztofowicz, R.: Probabilistic flood forecast : Exact and approximate predictive
844 distributions. *Journal of Hydrology*, 517(1), 643-651, 2014.
- 845 Kraller, G., Warscher, M., Strasser, U., Kunstmann, H., and Franz, H.: Distributed
846 hydrological modeling and model adaption in high alpine karst at regional scale



- 847 (berchtesgaden alps, germany). Springer International Publishing Switzerland.
848 https://doi.org/10.1007/978-3-319-06139-9_8, 2014.
- 849 Ladouche, B., Marechal, J. C., and Dorfliger, N.: Semi-distributed lumped model of a karst
850 system under active management. *Journal of Hydrology*, 509,215-230, 2014.
- 851 Li, J., Chen, Y., Wang, H., Qin, J., Li, J., and Chiao, S.: Extending flood forecasting lead
852 time in a large basin by coupling WRF QPF with a distributed hydrological model,
853 *Hydrol. Earth Syst. Sci.* 21, 1279–1294. <https://doi.org/10.5194/hess-21-1279-2017>,
854 2017.
- 855 Li, J., Yuan, D., Liu, J., Jiang, Y., Chen, Y., Hsu, K. L., and Sorooshian, S.: Predicting floods
856 in a large karst river basin by coupling PERSIANN-CCS QPEs with a physically based
857 distributed hydrological model. *Hydrol. Earth Syst. Sci.* 23, 1505-1532.
858 <https://doi.org/10.5194/hess-23-1505-2019>, 2019.
- 859 Li, J., Hong, A., Yuan, D., Jiang,Y., Deng,S., Cao,C., and Liu, J.: A new distributed
860 karst-tunnel hydrological model and tunnel hydrological effect simulations. *Journal of*
861 *Hydrology*, 593, 125639. <https://doi.org/10.1016/j.jhydrol.2020.125639>, 2020.
- 862 Li, J., Hong, A., Yuan, D., Jiang,Y., Zhang,Y., Deng,S., Cao,C., Liu, J., and Chen,Y.:
863 Elaborate Simulations and Forecasting of the Effects of Urbanization on Karst Flood
864 Events Using the Improved Karst-Liuxihe Model.CATENA,197,104990.
865 <https://doi.org/10.1016/j.catena.2020.104990>, 2021.
- 866 Liedl, R., Sauter, M., Huckinghaus, D., Clemens, T., and Teutsch, G.: Simulation of the
867 development of karst aquifers using a coupled continuum pipe flow model. *Water*
868 *Resources Research*, 39, 50-57, 2003.
- 869 Liu, X., Jiang, Y.J., Ye, M.Y., Yang, P.H., Hu, Z.Y., and Li, Y.Q.: Study on hydrologic regime
870 of underground river in typical karst valley- A case study on the Qingmuguan
871 subterranean stream in Chongqing. *CARSOLOGICA SINICA*, 28(2),149-154, 2009.
- 872 Lu, D. B., Shi, Z. T., Gu, S. X., and Zeng, J. J.: Application of Hydrological Model in the
873 Karst Area. *Water-saving irrigation*.11, 31-34. [doi:1007-4929\(2013\)11-031-04](https://doi.org/10.1007-4929(2013)11-031-04), 2013.



- 874 Mario, T.P., Daniel, B., Steven, A. M., Gabriele, C., and Barbara, W.: Bayesian calibration
875 and sensitivity analysis for a karst aquifer model using active subspaces. *Water*
876 *Resources Research*, 55,342-356. doi: [10.1029/2019WR024739](https://doi.org/10.1029/2019WR024739), 2019.
- 877 Meng, H.H., and Wang, N.C.: Advances in the study of hydrological models in karst basin.
878 *Progress in Geography*, 29,1311-1318, 2010.
- 879 Pan, H.Y.: Hydrological model and application in karst watersheds. China University of
880 Geosciences. Doctoral Dissertation, Wuhan, China, 2014.
- 881 Peterson, E.W., and Wicks, C. M.: Assessing the importance of conduit geometry and
882 physical parameters in karst systems using the storm water management model
883 (SWMM). *Journal of Hydrology*, 329, 1-2, 294-305, 2006.
- 884 Peterson, J.R., and Hamlett, J.M.: Hydrologic calibration of the SWAT model in a basin
885 containing fragipan soils. *JAWRA Journal of the American Water Resources*
886 *Association*. doi: [10.1111/j.1752-1688.1998.tb00952.x](https://doi.org/10.1111/j.1752-1688.1998.tb00952.x), 1998.
- 887 Petrie, R., Denvil, S., Ames, S., et al.: Coordinating an operational data distribution network
888 for CMIP6 data, *Geosci. Model Dev.*, 14, 629–644,
889 <https://doi.org/10.5194/gmd-14-629-2021>, 2021.
- 890 Qin, J.G., and Jiang, Y.P.: A review of numerical simulation methods for CFP pipeline flow.
891 *Groundwater*. 3, 98-100, 2014.
- 892 Reimann, T., Melissa, E., and Hill.: Modflow-cfp: a new conduit flow process for
893 modflow–2005. *Ground Water*,47(3),321-325. doi:[10.1111/j.1745-6584.2009.00561.x](https://doi.org/10.1111/j.1745-6584.2009.00561.x),
894 2009.
- 895 Ren, Q.W.: Water Quantity Evaluation Methodology Based on Modified SWAT
896 Hydrological Modeling in Southwest Karst Area, China University of Geoscience,
897 Wuhan, China, 2006.
- 898 Shoemaker, W.B., Cunningham, K.J., and Kuniansky, E.L.: Effects of turbulence on
899 hydraulic heads and parameter sensitivities in preferential groundwater flow layers.



- 900 Water Resources Research, 44, 34-50. doi: [10.1029/2007WR006601](https://doi.org/10.1029/2007WR006601), 2008.
- 901 Suo, L.T., Wan, J.W., and Lu, X.W.: Improvement and application of TOPMODEL in karst
902 region. *Carsologica Sinica*, 26(1), 67-70, 2007.
- 903 Williams, P. W.: Book Review: Methods in Karst Hydrogeology, Nico Goldscheider and
904 David Drew (eds). *Hydrogeology Journal*, 17,1025-1025, 2009.
- 905 Worthington, S., Ford, D., and Beddows, P.: Porosity and permeability enhancement in
906 unconfined carbonate aquifers as a result of solution. *Speleogenesis: evolution of karst*
907 *aquifers*, 2000.
- 908 Yang, P. H., Luo, J.Y., Peng, W., Xia, K.S., and Lin, Y.S.: Application of online technique in
909 tracer test-A case in Qingmuguan subterranean river system, Chongqing, China.
910 *CARSOLOGICA SINICA*, 27(3),215-220, 2008.
- 911 Yu, D., Yin, J., Wilby, R.L., Stuart, N. L., Jeroen, C., Lin, N., Liu, M., Yuan, H., Chen, J.,
912 Christel, P., Guan, M., Avinoam, B., Charlie, W. D., Tang, X., Yu, L., and Xu, S.:
913 Disruption of emergency response to vulnerable populations during floods. *Nature*
914 *Sustainability*, 3, 728–736. <https://doi.org/10.1038/s41893-020-0516-7>, 2020.
- 915 Yu, Q., Yang, P.H., Yu, Z.L., Chen, X.B., and Wu, H.: Dominant factors controlling
916 hydrochemical variation of karst underground river in different period,
917 Qingmuguan,Chongqing. *CARSOLOGICA SINICA*, 35(2),134-143, 2016.
- 918 Zhang, Q.: Assesment on the intrinsic vulnerability of karst groundwater source in the
919 Qingmuguan karst valley. *CARSOLOGICA SINICA*, 31(1),67-73, 2012.
- 920 Zhu, C., and Li, Y.: Long-Term Hydrological Impacts of Land Use/Land Cover Change
921 From 1984 to 2010 in the Little River Basin, Tennessee. *International Soil and Water*
922 *Conservation Research*, 2(2), 11-21, 2014.
- 923



924 **Tables**

925 Table 1 Parameters of the QMG model.

Parameters	Variable name	Physical property
Infiltration coefficient	I_c	Meteorology
Evaporation coefficient	λ	Vegetation cover
Soil thickness	h	Karst aquifer
Soil coefficient	S_b	Soil type
Saturated water content	S_c	Soil type
Rock porosity	R_p	Karst aquifer
Field capacity	F_c	Soil type
Permeability coefficient	K	Karst aquifer
Flow direction	F_d	Landform
Slope	S_o	Landform
Specific yield	S_y	Karst aquifer
Channel roughness	n	Landform

926 Table 2 Parametric sensitivity results in QMG model.

Infiltration coefficient/ I_c	Evaporation coefficient/ λ	Thickness/ h	Soil coefficient/ S_b	Saturated water content/ S_c	Specific yield/ S_y
0.92	0.24	0.71	0.58	0.8	0.83
Flow direction/ F_d	Slope/ S_o	Rock porosity/ R_p	Field capacity/ F_c	Permeability coefficient/ K	Channel roughness/ n
0.74	0.68	0.86	0.78	0.89	0.36

927 Table 3 Flood simulation evaluation index through parametric optimization.

Parameter optimization	Parameter types	Nash coefficient	Correlation coefficient	Relative flow process error/%	Flood peak error/%	Water balance coefficient	Peak time error (hours)
calibration	initial	0.82	0.77	24	29	0.82	4
periods	optimized	0.91	0.94	14	12	0.95	2
validation	initial	0.79	0.71	29	32	0.77	6
periods	optimized	0.88	0.87	18	16	0.92	3
average	initial	0.81	0.74	27	31	0.80	5
value	optimized	0.90	0.91	16	14	0.94	3

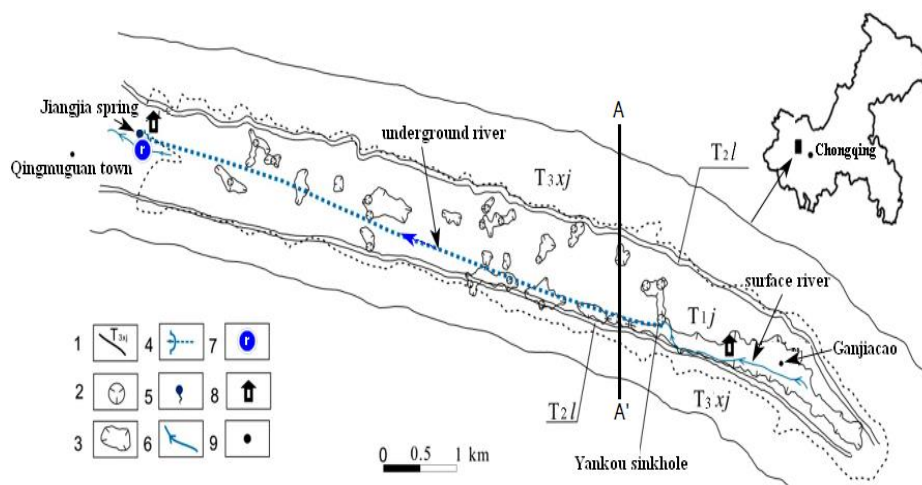


928 Table 4 Flood simulation indices for model validation.

Floods	Parameter types	Nash coefficient	Correlation coefficient	Relative flow process error/%	Flood peak error/%	Water balance coefficient	Peak time error/(hours)
2017042408	initial	0.77	0.7	28	29	0.71	-5
	optimized	0.95	0.89	11	15	0.88	-2
2017050816	initial	0.78	0.71	19	19	0.76	-4
	optimized	0.92	0.88	11	9	0.94	-2
2017061518	initial	0.76	0.6	25	32	0.63	-5
	optimized	0.91	0.93	12	11	0.95	-3
2017071015	initial	0.78	0.82	25	37	0.64	-4
	optimized	0.92	0.87	8	7	0.94	-2
2017091512	initial	0.81	0.62	21	16	0.78	-5
	optimized	0.9	0.92	13	10	0.9	-4
2017100815	initial	0.75	0.68	30	26	0.62	-2
	optimized	0.94	0.86	11	15	0.92	-1
2018052016	initial	0.78	0.68	25	21	0.67	5
	optimized	0.91	0.93	10	13	0.94	2
2018060815	initial	0.82	0.79	27	22	0.69	-6
	optimized	0.9	0.92	11	12	0.93	-4
2018071212	initial	0.84	0.75	26	24	0.61	5
	optimized	0.91	0.88	8	15	0.92	3
2018081512	initial	0.71	0.78	26	24	0.78	-4
	optimized	0.89	0.94	12	11	0.89	-3
2018090516	initial	0.85	0.68	28	23	0.68	-5
	optimized	0.93	0.87	12	10	0.92	-2
2018092514	initial	0.79	0.78	23	19	0.59	5
	optimized	0.88	0.88	9	11	0.89	2
2018101208	initial	0.78	0.81	28	25	0.63	5
	optimized	0.92	0.94	11	10	0.94	2
2018111208	initial	0.79	0.81	25	24	0.65	-6
	optimized	0.94	0.86	13	12	0.92	-2
2019042512	initial	0.78	0.8	26	36	0.8	5
	optimized	0.89	0.94	9	16	0.93	2
2019051513	initial	0.84	0.77	32	27	0.79	4
	optimized	0.91	0.88	9	13	0.95	2
2019052516	initial	0.74	0.75	29	26	0.63	-5
	optimized	0.92	0.86	7	15	0.96	-2
2019060518	initial	0.85	0.83	28	25	0.78	-4
	optimized	0.95	0.96	10	12	0.92	-2
average value	initial	0.79	0.74	26	25	0.69	5
	optimized	0.92	0.9	10	11	0.92	2



929 **Figures**

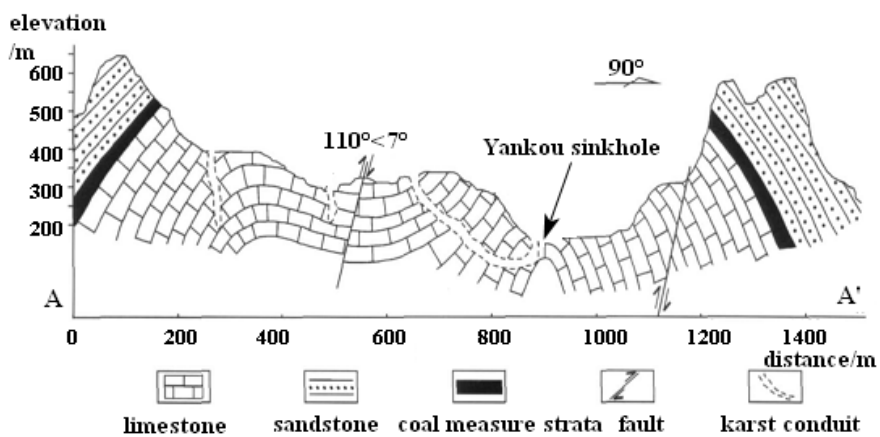


930

931 1- stratigraphic boundary, 2- sinkhole, 3- karst depression, 4- underground river, 5-
 932 karst spring, 6- surface river, 7- river gauge, 8- rain gauge, and 9- geographical name

933

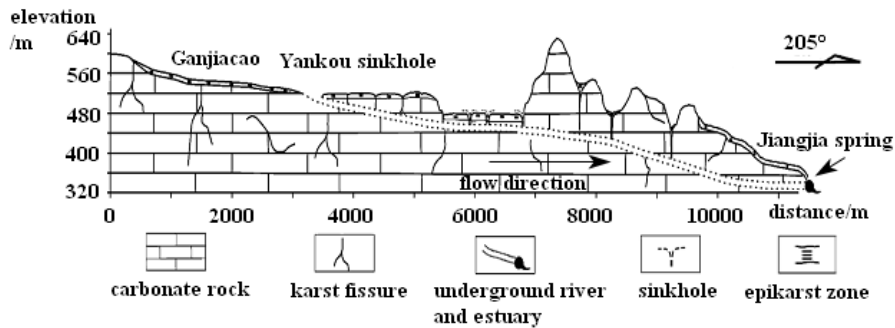
a. Qingmuguan karst basin (modified from Yu et al., 2016)



934

935

b. Lithologic cross section of Yankou sinkhole/AA'(modified from Zhang, 2012)



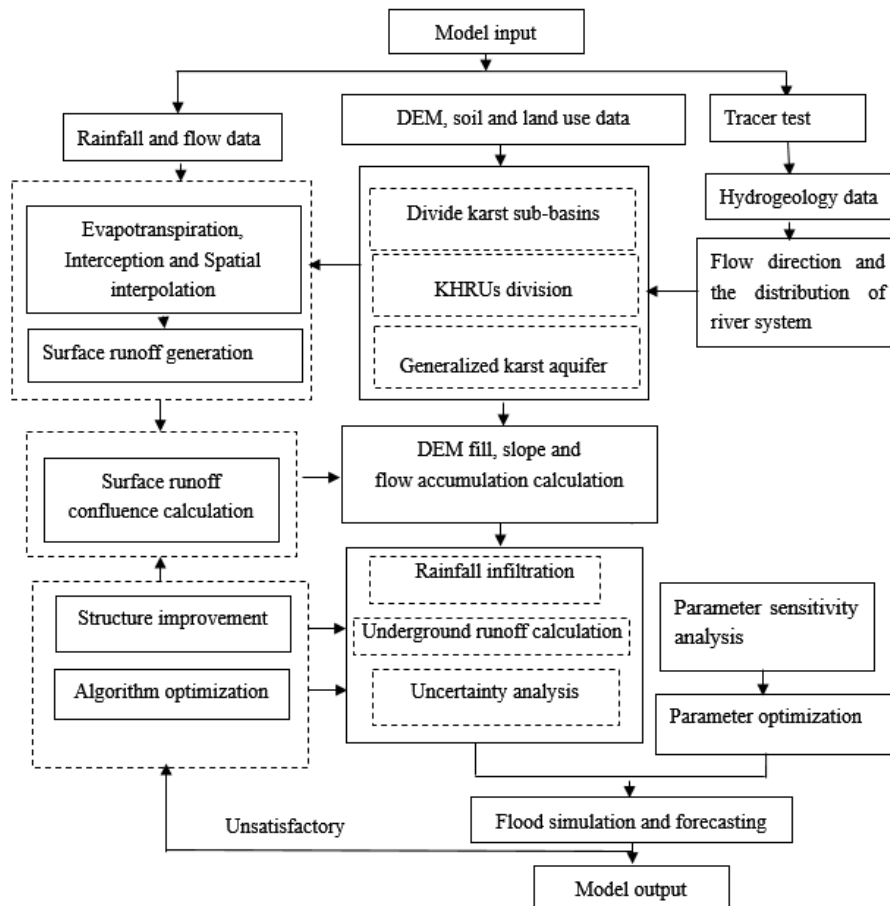
936

937

c. Longitudinal profile of the study area (modified from Yang et al., 2008)

938

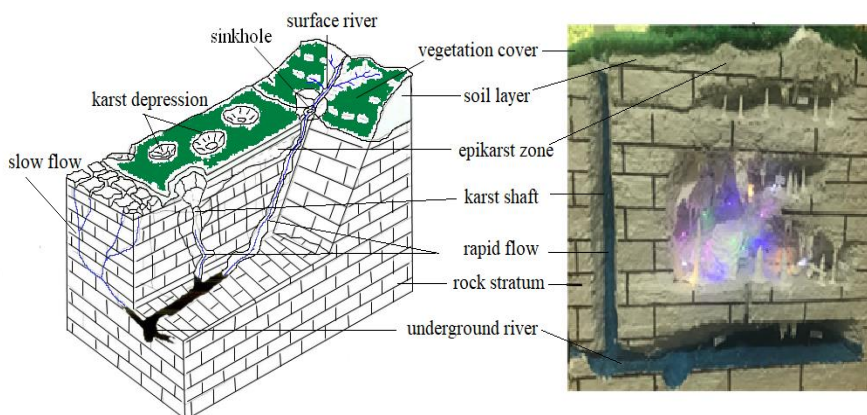
Figure 1 The Qingmuguan karst basin.



939

940

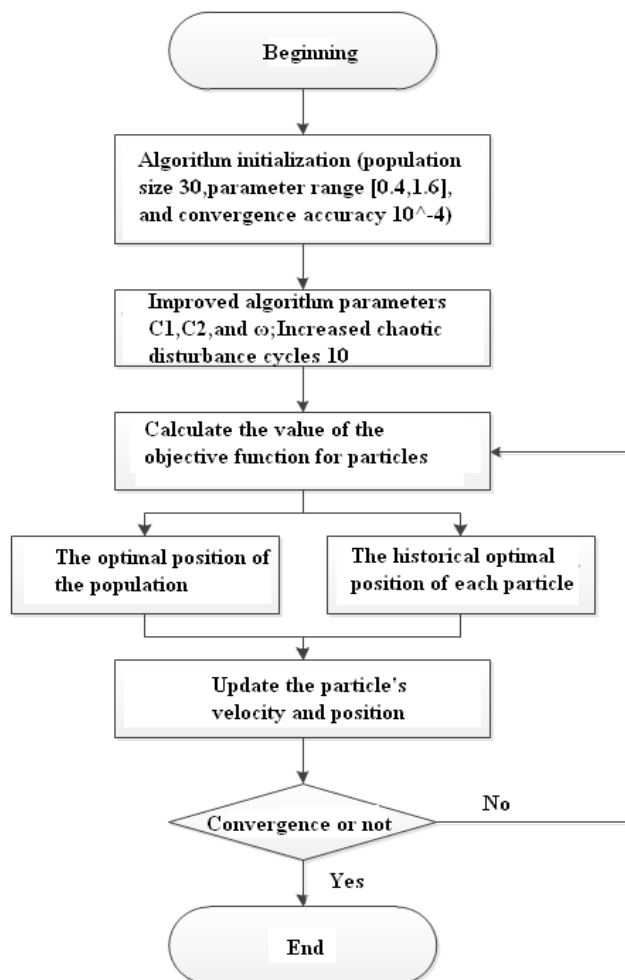
Figure 2 Modeling flow chart of QMG (Qingmuguan) model.



941

942

Figure 3 Spatial structure of the KHRUs (Li et al.,2021).

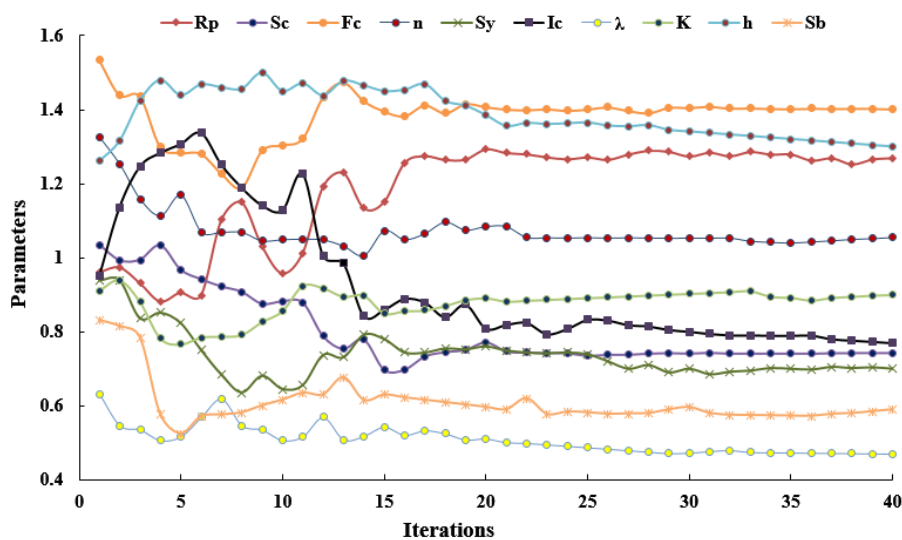


943



944

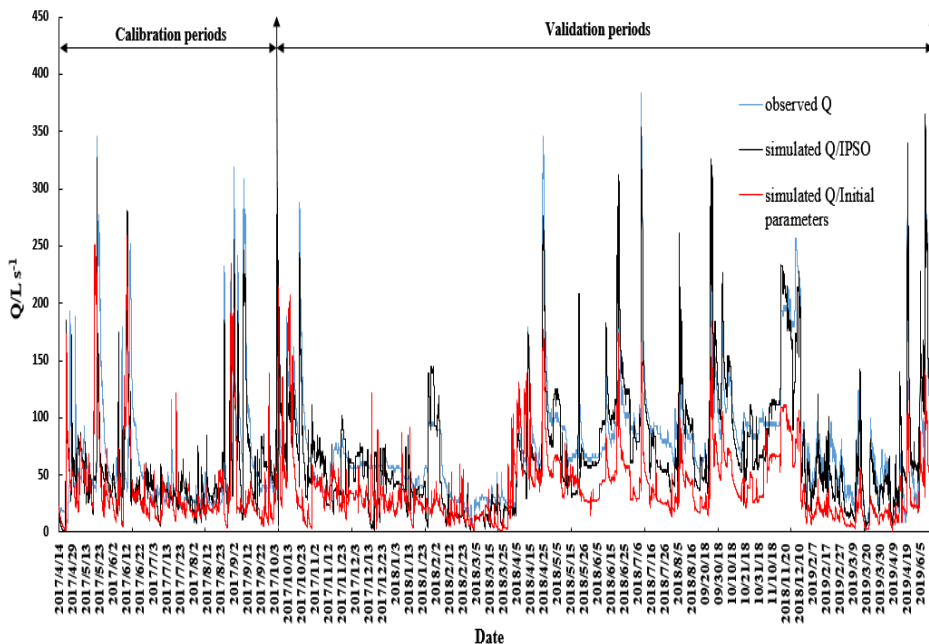
Figure 4 Algorithm flow chart of the IPSO.



945

946

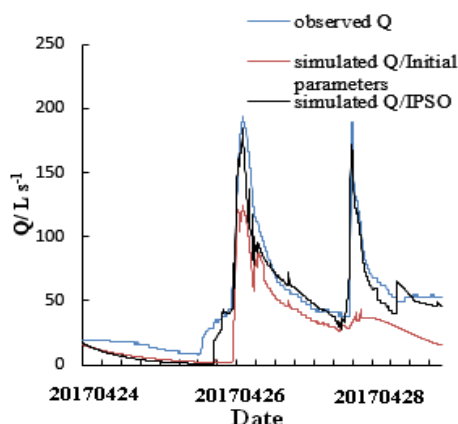
Figure 5 Iteration process of parametric optimization.



947

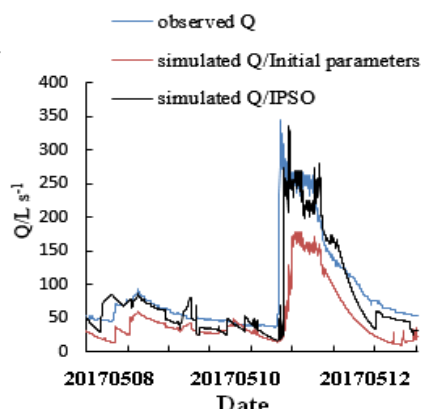
948

Figure 6 Flow simulation results of QMG model based on parameter optimization.

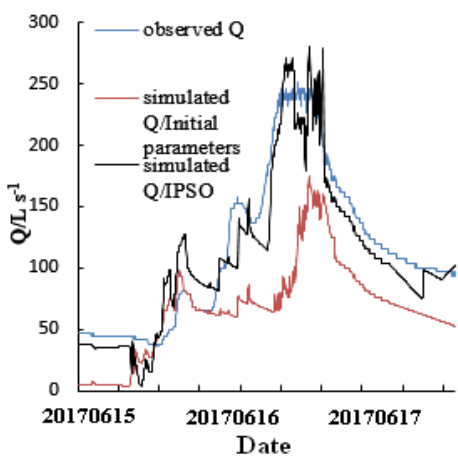


949
950

a. flood 201704240800

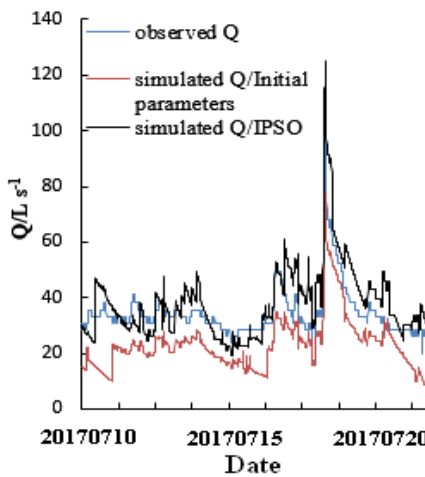


b. flood 201705081600

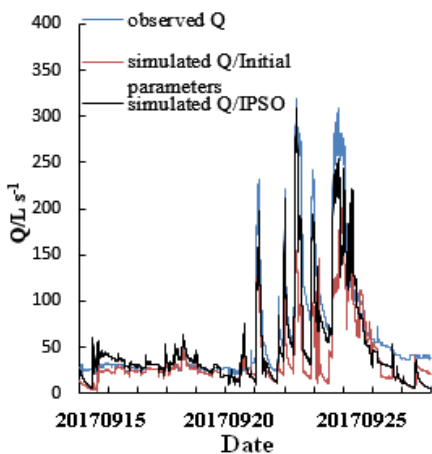


951
952

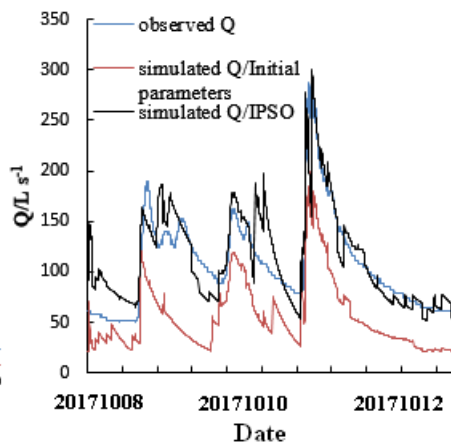
c. flood 201706151800



d. flood 201707101530

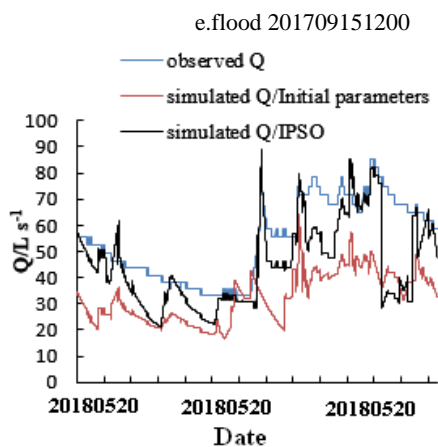


953

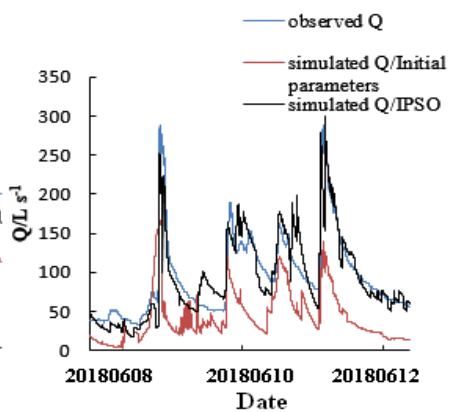




954



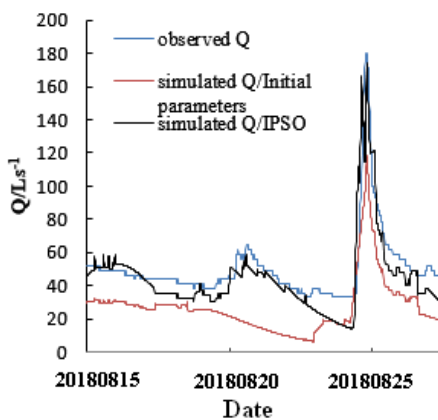
f.flood 201710081500



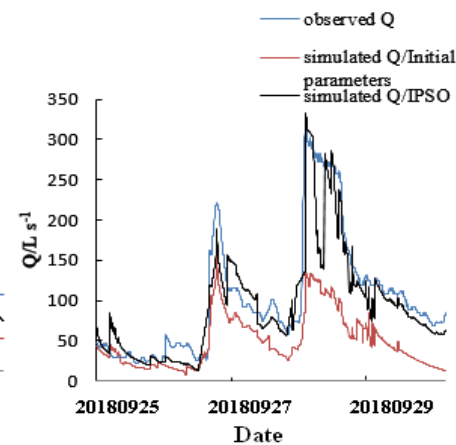
955

956

g.flood 201805201600



h.flood 201806081500



957

958

959

i.flood 201808151200

j.flood 201905251600

Figure 7 Flood simulation effects based on initial and optimized parameters.